Phononic thin plates with embedded acoustic black holes

Hongfei Zhu* and Fabio Semperlotti†

Department of Aerospace and Mechanical Engineering, University of Notre Dame, Notre Dame, Indiana 46556, USA

(Received 8 July 2014; revised manuscript received 1 March 2015; published 20 March 2015)

We introduce a class of two-dimensional nonresonant single-phase phononic materials and investigate its peculiar dispersion characteristics. The material consists of a thin platelike structure with an embedded periodic lattice of acoustic black holes. The use of these periodic tapers allows achieving remarkable dispersion properties such as zero group velocity in the fundamental modes, negative group refraction index, birefraction, Dirac-like cones, and mode anisotropy. The dispersion properties are numerically investigated using both a three-dimensional supercell plane wave expansion method and finite element analysis. The effect on the dispersion and propagation characteristics of key geometric parameters of the black hole, such as the taper profile and the residual thickness, are also explored.

DOI: 10.1103/PhysRevB.91.104304 PACS number(s): 43.35.+d, 46.40.Cd

I. INTRODUCTION

Phononic crystals (PCs) are an artificial medium made of two or more materials combined together to form a periodic structure. These materials offer unusual wave propagation characteristics such as acoustic band gaps [1–5], localized and guided defect modes [6–8], filtering of acoustic waves [9–11], acoustic lenses [12–14], and negative refraction [15,16], that are typically not achievable in conventional materials. PCs are often classified in two categories, nonresonant and locally resonant [17], in order to highlight the difference between their operating modes. The locally resonant materials exhibit low-frequency resonances (typically in the metamaterial range) localized at the inclusion while the nonresonant materials exhibit resonances of the inclusions only in the high-frequency range. Owing to this mechanism, the wave propagation characteristics in the low-frequency range are mostly impedance-driven for the nonresonant materials and inertia-driven for the locally resonant materials. These local resonances have been shown to be strictly related to the generation of negative effective properties (such as density and bulk modulus), which are at the basis of double negative properties [18].

Despite such remarkable dynamic properties, extensive integration of these materials into practical devices is still lacking. The fabrication complexity (particularly for the locally resonant type) and the nonstructural character (i.e., the fact that these materials are typically not load-bearing) of conventional PC designs are among the main limiting factors. In addition, the existence of numerous interfaces between dissimilar materials or internal structures drastically affects the overall load-bearing capability, the integrity, and the structural endurance of the host mechanical system.

In this study, we propose a class of two-dimensional structural PCs obtained by tailoring the geometry of a single-phase isotropic material able to provide the same high-level characteristics of locally resonant PCs. These materials are synthesized by embedding a periodic lattice of carefully engineered geometric inhomogeneities consisting of tapered holes. These inhomogeneities can be (virtually) introduced in any material by simply manufacturing tapers having prescribed profiles. This approach would potentially allow turning any material (amenable to thickness tailoring) into a metamaterial. Among the fabrication advantages of this design, we highlight that it does not require any interface between multiple materials and it can be retrofitted even to existing structures. This could have critical implications, for instance, in the development of highly absorbing thin-walled structures with embedded passive vibration and acoustic control capabilities. The proposed phononic structure (Fig. 1) consists of a thin plate made of a periodic lattice of exponential-like circular tapers, often referred to as acoustic black holes (ABH).

The physical principle exploited in ABHs was first observed by Pekeris [19] for waves propagating in stratified fluids and later extended to acoustics in solids by Mironov [20]. Mironov observed that, under certain conditions, flexural waves propagating in a thin plate with an exponentially tapered edge will theoretically never reflect back, therefore resulting in the so-called *zero reflection* condition. More recently, Krylov [21,22] exploited this concept to achieve passive vibration control of structural elements, coining the term acoustic black hole. The ABH consists in a variable thickness exponential-like circular taper able to produce a progressive reduction of the phase and group velocity as the wave approaches the center of the hole. Typical thickness profiles are of the form $h(x) = \varepsilon x^m$, where $\{m, \varepsilon\} \in \mathbb{R}$, $m \geqslant 2$, and $\varepsilon \ll (3\rho\omega^2/E)^{1/2}$ to satisfy the smoothness criterion [20,23]. In ideal ABH tapers, where the thickness decreases to zero, the phase and group velocities tend to zero as they approach the center of the ABH. Under this condition, the wave never reaches the center of the hole therefore the reflection coefficient approaches zero (the wave is not reflected back) and the hole appears as an ideal absorber. Energy balance considerations show that, in the absence of damping, the center of the hole becomes a point of singularity for both the particle displacement [20] and the vibrational energy [24]. In practice, the residual thickness at the center of the ABH cannot be made zero due to both fabrication and structural constraints. In the absence of damping, even the existence of a small residual thickness (compared with the full thickness of the plate) can produce appreciable levels of reflected energy (up to 70% [20]). Nevertheless, considerable wave speed reduction will still take place.

*hongfei.zhu.44@nd.edu
†fabio.semperlotti.1@nd.edu

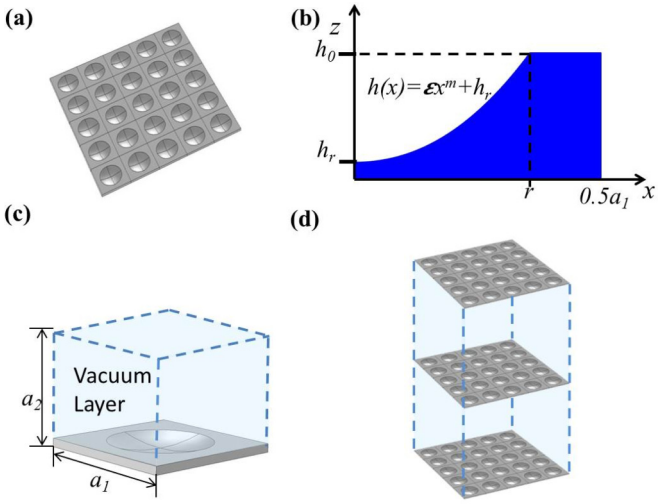

FIG. 1. (Color online) (a) Schematic of the phononic thin plate with a square ABH periodic lattice structure, (b) cross section of the acoustic black hole showing the taper profile, (c) 3D supercell used for the PWE model made by the combination of the plate unit cell and by a thick vacuum layer, and (d) the assembled 3D structure obtained by alternating the ABH plates and the vacuum layers.

II. NUMERICAL MODEL

We consider an infinite thin plate with a periodic distribution of ABH-like tapers forming a square lattice as shown in Fig. 1(a). The plate has thickness $h_0 = 0.008$ m and a taper profile $h(x) = \varepsilon x^m + h_r$, where h_r is the residual thickness as shown in Fig. 1(b).

The elastodynamic response of the phononic thin plate is governed by the Navier's equations:

$$\rho \frac{\partial^2 u_i}{\partial t^2} = (C_{ijkl} u_{k,l})_{,j}, \qquad i = 1,2,3, \tag{1}$$

where ρ is the density, C_{ijkl} is the stiffness tensor, and u_i are the components of the displacement field. Equation (1) is also subjected to traction-free boundary conditions $\vec{T} = \sigma(\vec{r}) \cdot \vec{n}(\vec{r}) = 0$ at the upper and lower surfaces, where $\vec{n}(\vec{r})$ is the normal vector to the surface, $\sigma(\vec{r})$ is the local stress tensor, and $\vec{r}$ the position vector from the center of the ABH. The boundary conditions are applied at $z = 0$ on the bottom surface and at $z = h(x)$ if $0 \leqslant x \leqslant r$ or at $z = h_0$ if $r \leqslant x \leqslant 0.5a_1$ on the top surface.

The dispersion relations are obtained from Eq. (1) by using a three-dimensional supercell plane wave expansion (PWE) approach [25]. According to this methodology, a supercell made of the combined thin plate unit cell and of a vacuum layer is first assembled [Fig. 1(c)]. The periodicity is then enforced in the three coordinate directions resulting in the 2D periodic thin plate of interest and in a series of mirror images in the z direction. The vacuum layer ensures that these mirror images are dynamically decoupled from each other and simply result in repeated roots when solving the dispersion relations.

This modeling approach was selected because it allows a much easier treatment of the traction-free boundary conditions of the tapered thin plate. In fact, with the supercell approach, the initial traction-free surfaces in the thin plate become internal interfaces between the plate and the vacuum layer therefore removing the need to impose explicitly the boundary conditions. The model is virtually converted from a thin plate into an infinite medium made of alternated metamaterial and vacuum layers. At this stage, the material properties can be approximated using a three-dimensional Fourier series expansion. We highlight that this approach does not have any physical implication and it is used only to simplify the numerical modeling.

In order to solve Eq. (1), the position dependent density $\rho(\vec{r})$ and elastic coefficients $C_{ijkl}(\vec{r})$ are expanded in Fourier series using the reciprocity vector $\vec{G} = (G_x, G_y, G_z)$:

$$C_{ijkl}(\vec{r}) = \sum_G e^{i\vec{G}\bullet\vec{r}} C_{ijkl\,G} \tag{2}$$

and

$$\rho(\vec{r}) = \sum_G e^{i\vec{G}\bullet\vec{r}} \rho_G, \tag{3}$$

where ρ_G and $C_{ijkl\,G}$ are the corresponding 3D Fourier coefficients and are defined as

$$C_{ijkl\,G} = \frac{1}{V} \int_V C_{ijkl}(\vec{r}) e^{-i\vec{G}\bullet\vec{r}} dr^3 \tag{4}$$

and

$$\rho_G = \frac{1}{V} \int_V \rho(\vec{r}) e^{-i\vec{G}\bullet\vec{r}} dr^3 \tag{5}$$

In the following analysis, the Fourier coefficients in Eqs. (4) and (5) can be reduced to the single integral as

$$\alpha_G = \begin{cases} \frac{\alpha}{a_1^2 a_2} \left[\int_{h_r}^{h_0} \left(a_1^2 - \pi r(z)^2\right) e^{-iG_z z} dz + \int_0^{h_r} a_1^2 e^{-iG_z z} dz \right] & \text{if} \quad (G_x, G_y) = 0, \\ \frac{\alpha}{a_1^2 a_2} \left[\int_{h_r}^{h_0} \frac{-2\pi r(z)^2 J_1\left(\sqrt{G_x^2+G_y^2} r(z)\right)}{\sqrt{G_x^2+G_y^2} r(z)} e^{-iG_z z} dz \right] & \text{if} \quad (G_x, G_y) \neq 0, \end{cases} \tag{6}$$

where $\alpha = (\rho, C_{ijkl})$ and $r(z) = \left(\frac{z-h_r}{\varepsilon}\right)^{\frac{1}{m}}$ and the single integrals are calculated via numerical integration using the Simpson method.

Upon using the Bloch theorem and expanding the displacement vector $\vec{u}(x,y,z,t)$ in Fourier series, we obtain

$$\vec{u}(\vec{r}) = \sum_{G'} A_{G'} e^{i[(\vec{k}+\vec{G}')\cdot\vec{r} - \omega t]}, \tag{7}$$

where $\vec{k} = (k_x, k_y, 0)$ is the Bloch plane wave vector, ω is the circular frequency, and $A_{G'}$ is the amplitude of the displacement vector. Substituting Eqs. (2), (3), and (7) into Eq. (1) and collecting terms, we obtain the $3n \times 3n$ set of equations:

$$\begin{pmatrix} C^{11}_{G,G'} & C^{12}_{G,G'} & C^{13}_{G,G'} \\ C^{21}_{G,G'} & C^{22}_{G,G'} & C^{23}_{G,G'} \\ C^{31}_{G,G'} & C^{32}_{G,G'} & C^{33}_{G,G'} \end{pmatrix} \begin{pmatrix} A^1_{G'} \\ A^2_{G'} \\ A^3_{G'} \end{pmatrix} = \omega^2 \begin{pmatrix} \rho_{G,G'} & 0 & 0 \\ 0 & \rho_{G,G'} & 0 \\ 0 & 0 & \rho_{G,G'} \end{pmatrix} \begin{pmatrix} A^1_{G'} \\ A^2_{G'} \\ A^3_{G'} \end{pmatrix}, \tag{8}$$

where the $n \times n$ submatrices $C_{G,G'}$ are functions of the Bloch wave vector $\vec{k}$, the reciprocal lattice vectors $\vec{G}$, the circular frequency ω, and the Fourier coefficients ρ_G and $C_{ijkl\,G}$. The detailed expression for the $n \times n$ sub-matrices $C_{G,G'}$ can be found in [25]. Equation (8) can be written in the form of an eigenvalue problem whose solution provides the eigenfrequencies and the eigenmodes of the system.

In the following numerical study, we consider a reference configuration consisting of a 0.008-m-thick aluminum plate with tapers characterized by $m = 2.2$, $\varepsilon = 5$, radius $r = 0.05$ m, and residual thickness $h_r = 0.0011$ m. The lattice has a square configuration with lattice constant $a_1 = 0.14$ m. The reciprocal lattice constants retained for the expansion are $G_x = G_y = \pm(6,5,4,3,2,1,0)2\pi/a_1$ and $G_z = \pm(3,2,1,0)2\pi/a_2$, where $a_2 = 0.064$ m. The selection of these reciprocal lattice vectors resulted from a convergence analysis (results not shown here) and was confirmed by direct comparison of the dispersion relation with finite element analysis. The constant a_2 was selected so to dynamically isolate the different slabs in the z direction.

III. DISPERSION RELATIONS AND GEOMETRIC ACOUSTIC ANALYSIS

The band structure along the boundary of the first Brillouin zone (BZ) for normalized frequencies $\Omega = \frac{\omega a_1}{2\pi C_t}$ up to 0.25 is shown in Fig. 2 where $C_t = \sqrt{\frac{C_{44}}{\rho}}$ is the bulk transverse velocity for aluminum.

The dispersion curves show several peculiar properties that are typically observable only in locally resonant materials. Several nonmonotonous branches can be found in the low-frequency range. In particular, for the fundamental nonmonotonous modes the same branch is associated with different mode types and group velocity regions. As an example, along the Γ-X boundary the S_0 mode evolves into the A_0 mode after crossing a zero group velocity point (ZGVP). Similar behavior is observed for the SH_0 mode that evolves into a higher order flexural mode along the Γ-X boundary. The ZGVP point also separates regions with positive and negative group velocity. It has long been known [26] that the higher order Lamb modes in plates can display zero group velocity points corresponding to waves having finite phase velocity but vanishing group velocity. However, the occurrence of this phenomenon is not common in fundamental Lamb modes. A similar behavior was previously observed only in phononic plates with pillar structures [27,28]. The ZGVP is related to the existence of a standing wave associated with a local resonance of the plate. The branch of the dispersion curve on the right of the ZGVP is characterized by negative group velocity which corresponds to backward wave propagation. The dispersion curves also reveal a remarkable coupling between the different mode types highlighting the existence of a phenomenon known as *mode hybridization* [29,30]. The change in the mode structure between the (A_0) and the (S_0) lamb modes occurs very rapidly in the neighborhood of the ZGVP.

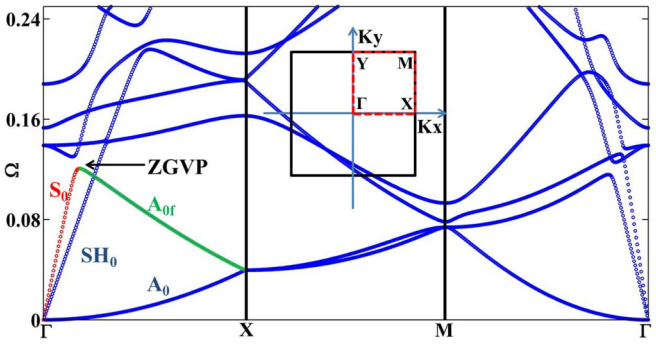

FIG. 2. (Color online) Dispersion curves along the irreducible part of the first Brillouin zone for the ABH phononic plate structure in reference configuration. The inset shows a schematic of the BZ for the square unit cell.

Several ZGVPs were also observed in the high-frequency limit. Although this phenomenon was previously observed both in phononic structures [29] as well as in homogeneous thin plates [26], we observe that the fundamental mechanism inducing the transition to negative group velocity is quite different. In conventional phononic plates, the high-frequency ZGVPs are induced by the mechanical impedance mismatch between the background and the inclusions which ultimately results in strong back-scattering effects. In ABH phononic plates, the transition to negative group velocity is due to the local inhomogeneity of the ABH cell that bends progressively the incoming wave. The inhomogeneity created by the geometric taper produces a spatially dependent phase velocity region that bends the acoustic ray in the direction of the decreasing phase velocity gradient, that is towards the ABH center. This mechanism was confirmed by performing a ray acoustic analysis of the single ABH unit.

The governing equations defining the ray trajectory of a bending wave inside a cylindrically symmetric tapered hole can be written (neglecting modes conversion) in the form [31]:

$$\frac{dr}{d\theta} = r\frac{1}{\tan\alpha}, \tag{9}$$

$$\frac{d\alpha}{d\theta} = -1 - \frac{r}{n}\frac{dn}{dr}, \tag{10}$$

$$nr\sin\alpha = \text{const}, \tag{11}$$

where r and θ are the coordinates of a polar system having origin at the ABH center, α is the angle between $\boldsymbol{r}$ and the wave vector $\boldsymbol{k}$, $n(r) = \sqrt{\frac{h(r)}{h_0}}$ is the local refraction index, and $h(r)$ is the local thickness. Note that these results are valid

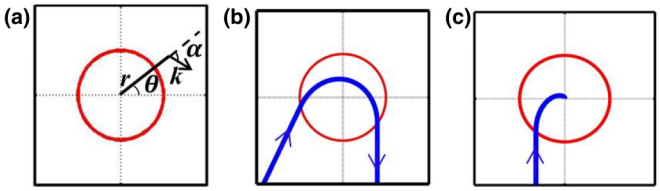

FIG. 3. (Color online) (a) Schematic of the unit cell and of the reference system used for the ray acoustic analysis. (b) and (c) show the results of geometric acoustic analysis illustrating the effect of different tapers on an incoming ray. (b) corresponds to the ray trajectory for the reference configuration showing that the ray is bent backward as it travels through the tapered area while (c) corresponds to an ideal ABH taper (i.e., $h_r \to 0$), which would produce full absorption of the incoming ray.

in the short-wavelength limit, which is assumed as that range where the wavelength of the incoming fundamental flexural mode $\lambda_{A_0} \leqslant r$, where r is the radius of the ABH.

Depending on the properties of the incoming ray and on the geometric characteristics of the taper, particularly the taper exponent and the residual thickness, the wave can be either 1) slowed down and captured by the ABH therefore contributing to the generation of a local resonance [Fig. 3(c)] or 2) bent in the backward direction [Fig. 3(b)]. In the short-wavelength limit, these conditions can be related to the generation of a ZGVP and to backward propagation, respectively.

IV. BI-REFRACTION PHENOMENON

To further understand the wave propagation characteristics of the ABH lattice structure, we calculated the equifrequency contours (EFC) for the fundamental nonmonotonous mode $S_0 - A_{0f}$ (Fig. 4). Results highlight the existence, in the same band, of a dual EFC contour associated with different group velocity directions. This aspect is of particular interest because it was shown in previous studies [29,32] to be a fundamental condition for the existence of birefraction.

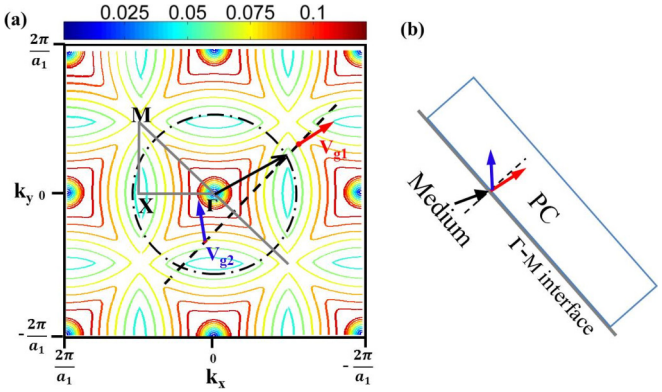

FIG. 4. (Color online) (a) EFC for the fundamental non-monotonous mode $S_0 - A_{0f}$. The black arrow and the black dashed line indicate the incident wave vector and the conservation line, respectively. The red arrows indicate the direction of the refracted waves. The black dashed circle represents the EFC of an incident wave propagating in a homogeneous flat plate. (b) Schematic of the birefraction mechanism.

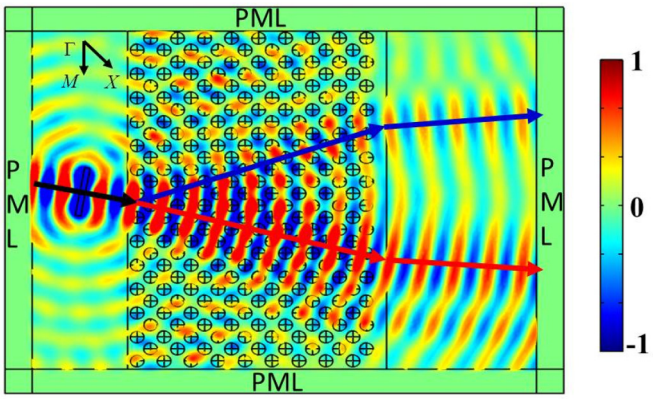

FIG. 5. (Color online) Full field simulations illustrating the positive-negative bi-refraction phenomenon. The incident wave was emitted from a line source oriented at a 10° angle with respect to the ABH slab and impinging along the Γ-M interface of the ABH lattice. The wave front emerging from the ABH slab clearly show the occurrence of the bi-refraction effect (red and blue arrows).

To illustrate this phenomenon, we superimpose the EFC corresponding to an incident wave at a fixed frequency propagating in a homogeneous constant thickness plate (dashed black circle). The wave vector of the refracted beam must satisfy the $k_\parallel$-conservation relation [29] $k_\parallel^{\text{inc}} = k_\parallel^{\text{ref}} + G_\parallel$, where $k_\parallel^{\text{inc}}$ and $k_\parallel^{\text{ref}}$ are the components of the wave vector of the incident and refracted wave parallel to the interface, $G_\parallel$ is the parallel component of the reciprocal lattice vector. The group velocity is given by $V_g = \nabla\Omega(\vec{k})$, which is always perpendicular to the EFCs and pointing towards the direction of increasing frequency. In our case, dual EFCs with opposite group velocities co-exist at the same frequency, therefore bi-refraction should be expected. As shown in Fig. 4(a), Γ-M is assumed as the interface boundary and the black solid arrow represents the possible incident beam. The refracted beam are determined by finding the intersection point between the corresponding EFC and the conservation line (marked by the black dashed lines perpendicular to the Γ-M boundary). Since the refracted beams are in the direction of the group velocity at the crossing point (red and blue arrows), bi-refraction with positive-negative directions can be achieved. A full field simulation was performed to illustrate the transmission properties of the ABH material at these frequencies. An ABH slab aligned along Γ-M direction was embedded into an initially homogeneous thin aluminum plate. A flexural plane wave front was generated by a line source located in the flat plate and oriented at an angle of about 10° with respect to the ABH slab. The flexural wave was generated at the nondimensional frequency $\Omega = 0.0673$ corresponding to the bi-refraction region indicated by the EFC analysis. The numerical results (Fig. 5) clearly show the occurrence of the bi-refraction effect in the transmitted wave front emerging from the ABH slab.

V. EXISTENCE OF DEGENERATE POINTS AND DIRAC-LIKE CONES

Another interesting property of the ABH phononic plates is the existence of several degenerate points not only at the

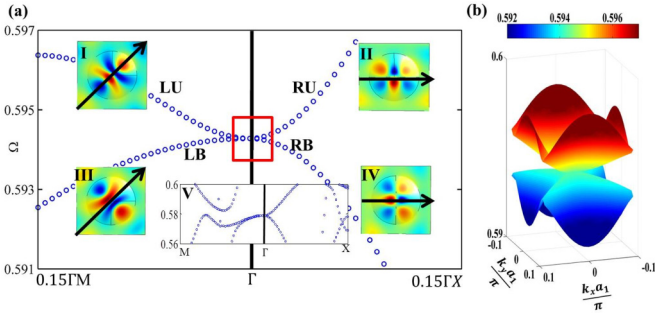

FIG. 6. (Color online) (a) Close-up view of the dispersion relations around $\Omega = 0.594$ showing the existence of a double degenerate singularity. The insets I–IV show the modal displacements corresponding to the modes labeled LU, RU, LB, and RB. The black arrow shows the wave vector direction. Inset V shows the dispersion relations when a small perturbation of the taper coefficient m is applied. The slight change in the geometric configuration makes the bell-like structure disappear while maintaining the degeneracy, therefore indicating that the characteristics of the EFCs are dominated by the geometric symmetry of the lattice structure. (b) shows the EFS contour around the degenerate point.

boundary but also at the center Γ of the BZ. The latter is of particular interest and deserves further attention. Each point results from the intersection of upper and lower branches where only a degenerate mode at $\vec{k} = 0$ exists. Both double and triple degeneracies were observed on the Γ point depending on the selection of the taper parameters and of the frequency range. We will show that, while the double degeneracy is associated with an interesting phenomenon of mode anisotropy, the triple degenerate point leads to the formation of Dirac-like cones (DC) [33–35] at the center of the BZ. An example of both types of degeneracies is reported here below.

Figure 6(a) shows an example of double degeneracy at the Γ point. The singularity around $\Omega = 0.594$ originates by the coalescence of two equifrequency surfaces (EFS). The dispersion relations in the neighborhood of the degenerate point are parabolic with zero slope at $\vec{k} = 0$, therefore indicating zero group velocity.

By analyzing the branches emanating from the singularity point (either along the Γ-X or the Γ-M boundary), we observe that they correspond to pairs of dissimilar flexural modes with different symmetry (see insets in Fig. 6(a) for the modal displacement pattern). The branches along the Γ-M boundary are characterized by a spurious dipole eigen-structure with mirrorlike symmetry, while branches along the Γ-X boundary exhibit a hexapole shape with a 90° rotation around the z axis.

A close-up view of the EFS around the degenerate point is shown in Fig. 6(b). Note that the shape of the lower branch clearly indicates anisotropic behavior while the upper branch (close to the singularity point) is a quasicircular cone, therefore suggesting quasi-isotropic characteristics in the selected frequency range. Each cone is composed of different modes in the different propagation directions, therefore indicating that the ABH-PC presents a peculiar *mode anisotropy* even in presence of quasi-isotropic dispersion behavior (upper branch). This concept is, in principle, analogous to the *super-anisotropy* characteristic previously observed in certain type of metamaterials [33] exhibiting degenerate singularities at the center of the BZ.

Unlike the superanisotropic metamaterials where the degenerate point was generated by accidental degeneracy [33], this type of double degeneracy appears to be induced by the symmetry of the ABH lattice structure. This observation is supported by the result shown in the inset (V) in Fig. 6(a) where a small perturbation of the ABH taper coefficient m from 2.2 to 2.5 (while keeping the remaining geometric parameters unchanged) destroys the conelike behavior while maintaining the degenerate point.

We highlight that this behavior is of particular interest due to the existence of an atypical mode anisotropy. The appearance of double degenerate points joining parabolic dispersion curves on the Γ point is common in many periodic materials. In fact, the parabolic nature of these curves follows from the time-reversal symmetry of the wave equation which imposes $\omega(-k) = \omega(k)$. However, this symmetry would also imply mode isotropy in the different directions which instead is clearly violated in our structure.

For a different selection of the geometric parameters, we also observed the occurrence of triple degeneracies with Dirac-Cone-like behavior. By changing the ABH taper coefficient to $m = 2.58$ (while leaving the remaining parameters unchanged), we identified triple degenerate points in the center of the BZ as shown in Fig. 7(a). Contrarily to the double degeneracy described above, this point at $\Omega_0 = 0.4212$ exhibits the typical Dirac-Cone-like behavior [see Fig. 7(b)] characterized by symmetry about the Dirac point (DP) and by locally linear dispersion. The linearity results in a constant and nonzero group velocity in the neighborhood of the DP, as opposed to the double degenerate case. Unlike the previously discussed degeneracy or the metamaterial configuration considered in Ref. [33], this DP was not associated with either mode anisotropy or superanisotropy. Also in contrast with the previous type of singularity, this triple point results from an accidental degeneracy [36]. This observation is confirmed by the results in Fig. 7(c) where, following a slight perturbation of the ABH taper (taper coefficient m changed from 2.58 to 3), the cones separate and the triple degenerate point splits into a nondegenerate and a double degenerate mode.

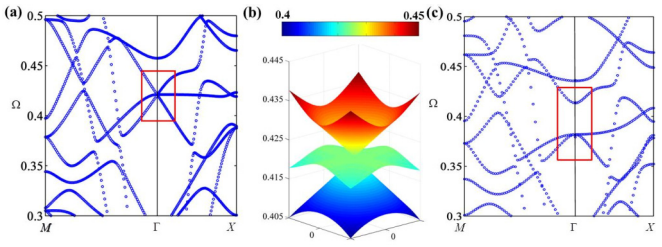

FIG. 7. (Color online) (a) The dispersion relations around $\Omega = 0.4212$ showing the existence of a triple-degenerate point and a Dirac Cone (red box) when the taper parameter is set to $m = 2.58$. (b) EFS plot around the DP showing the formation of the Dirac Cones. (c) When the geometric configuration is slightly perturbed (taper coefficient m changed from 2.58 to 3) the degenerate point and the DC disappear, therefore indicating that the triple point and the DC are due to an accidental degeneracy.

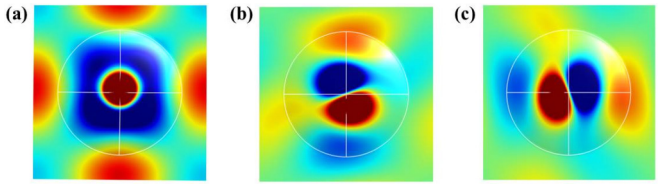

FIG. 8. (Color online) (a)–(c) show the field pattern of the eigenstates of the three degenerate modes near the DP.

Of particular interest are also the transmission properties of the phononic ABH material when excited at or in the neighborhood of the Dirac-like point [Fig. 7(a)]. Previous studies have already highlighted the existence of a wide range of peculiar transmission properties such as the zero-refractive-index material [33,36], the pseudodiffusive transmission [37,38], and the Zitterbewegung [39,40]. It was shown in Refs. [36,41] that in photonic crystals with square lattice geometry, the effective medium theory [42] could still be applied in the short wavelength limit if the triple degenerate state at the center of the BZ zone can be mapped to the superposition of monopole and dipole eigenstates. This study resulted in the observation that, at the Dirac Point, double zero-effective properties indicating diffusive instead of wavelike propagation can be achieved. Nevertheless, the effective theory approach was not applicable to the study of the DP in our ABH material because, beyond the fact that the DP point occurs in the high-frequency range ($\lambda_0 = 0.63a$ calculated from the A_0 mode in the background material), the analysis of the three degenerate eigenstates (Fig. 8) showed that the above conditions were not satisfied.

For the above reasons, the wave transport properties around the Dirac point were investigated by direct numerical simulations using the finite element model in Fig. 9(a). The structure consisted in a flat plate with an embedded slab of ABH material with geometric properties consistent with those of the ABH-PC configuration previously discussed. Perfectly matched layers were used at both the left and the right boundaries to avoid reflections while the top and bottom boundaries were treated with periodic BCs in order to simulate an infinite plate. The structure was excited by a flexural A_0 plane wave generated at the left boundary. The model was assembled and solved for the steady-state response using COMSOL MULTIPHYSICS.

Two excitation conditions were explored. The first condition consisted in a plane wave at a frequency $\Omega_1 = 1.0271\Omega_0$ off the DP but still in the linear dispersion range of the DC, while the second consisted in a plane wave at a frequency $\Omega_2 = 1.0088\Omega_0$, which is very close to the DP.

When the structure is excited at the Ω_1 we observe a planar wave emerging on the right-hand side of the ABH slab [Fig. 9(b)]. We already noted above that in this frequency range the ABH material cannot be mapped to a zero or near-zero effective property material, therefore the propagation inside the slab is still of wavelike type and the wave front reconstruction mechanism is mostly controlled by scattering effects. As a further demonstration of this mechanism we explored the response of the same flat plate configuration when a defect [the circular through hole labeled "i" in Fig. 9(a)] is introduced in the ABH slab. The response shown in Fig. 9(d)

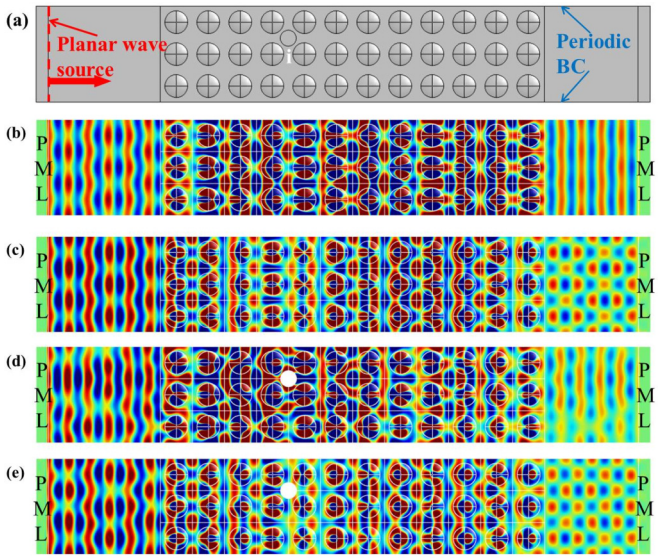

FIG. 9. (Color online) (a) Schematic of the model used to investigate the wave transport properties around the Dirac Point in the ABH-PC plate. The plate has perfectly matched layers on the left and right boundaries and periodic boundary conditions on the top and bottom boundaries. The excitation consists in a flexural plane harmonic wave generated at the left boundary. The element labeled (i) indicates the location of a structural defect consisting in a through hole. The response of the plate is shown in terms of the flexural displacement field generated at steady state in the intact plate at a frequency (b) $\Omega_1 = 1.0271\Omega_0$, which shows the occurrence of a planar wave reconstruction behavior, and at a frequency (c) $\Omega_2 = 1.0088\Omega_0$, which shows the occurrence of the Talbot effect. (d) and (e) show the same response when the propagation occurs in the defected plates with defect located at i. The analysis of the transmitted field shows that the Talbot effect is able to induce defect immunity while the planar wave front transmission is altered by the presence of the defect as it should be expected in absence of double zero-effective properties.

where the emerging wave front is clearly distorted by the presence of the defect. This behavior is opposed to what expected if the slab exhibited a diffusive propagation behavior which would lead to the defect being undetectable from the downstream field, a condition referred to as *defect immunity*.

The second interesting wave transport phenomenon was observed when exciting the ABH slab at frequency Ω_2 that is closer to the DP, as previously mentioned. Results [Fig. 9(c)] show the existence of the so-called *Talbot effect* [43] that consists in a near-field diffraction mechanism. According to this effect, a plane wave propagating through a finite slab of the periodic material is modified so that the emerging wave (on the other side of the slab) replicates the periodic geometry of the slab itself. The numerical results in Fig. 9(c) clearly show the presence of the Talbot effect which alters the transmitted field according to the lattice geometry. One interesting characteristics of the Talbot effect is the insensitivity to defects in the lattice structure. This property is illustrated by propagating the same plane wave through a periodic slab with an internal defect. Results [Fig. 9(e)] show that the scattered field from the defect cannot be detected from the analysis of the transmitted wave field therefore confirming the defect

immunity ability associated with Talbot effect. We note that a similar transmission behavior was also reported at frequencies close to a doubly degenerate DC in honeycomb lattice PC made of iron inclusions embedded in water [44]. The inability to describe the current material in the high-frequency range of interest for the DP via the effective medium theory does not allow to gain further insight into the fundamental mechanism at the basis of the wave reconstruction and the Talbot effect. An approach based on group theory or multiple scattering might be able to provide further insight, although the development of these modeling tools for tapered structures would require a dedicated study which is beyond the scope of this letter.

VI. PARAMETRIC ANALYSIS

It was previously mentioned that the different properties and coupling mechanisms observed in ABH metamaterials strongly depend on the geometric parameters of the taper, namely the residual thickness and the taper exponent. It is therefore important to study how the band structure develops and how the different modes are affected by the design parameters. Due to the complexity of the structure, we explored this dependence via a parametric analysis. Figure 10 shows the evolution of the dispersion relations with the residual thickness. Figures 10(a)–10(c) correspond to different residual thickness cases where the coefficients ε are set to 1, 3, and 5 meaning that the hole geometry varies from shallow to deep. Figure 10(a) represents the shallow hole case ($h_r = 0.006\,26$) where the effects of the ABH should be less evident. As expected, the dispersion curves are quite similar to those of guided waves in a flat plate. In the low-frequency range, we observe the S_0, SH_0, and A_0 modes and several folded branches of the A_0 mode due to the folding effect induced by the periodicity. The only significant difference is observed in correspondence to the mode crossing points. At these points, we observe splitting of the original modes and the generation of the nonmonotonous hybrid modes connected by the ZGVP. The remaining part of the dispersion relations is essentially unaffected. By increasing the ABH slope [Figs. 10(b) and 10(c)], the splitting and hybridization mechanisms become more evident even at higher frequency. A physical interpretation of this anomalous dispersion can be made in term of the coupled-wave theory [45]. When two modes are coupled by a distributed mechanism (in our case the periodic inhomogeneity created by the ABH taper), significant interaction only occurs at synchronism, that is,

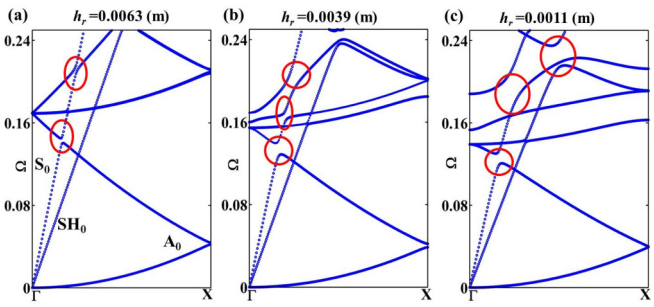

FIG. 10. (Color online) Dispersion relations for different residual thickness values: (a) $h_r = 0.0063$, (b) 0.0039, and (c) 0.0011.

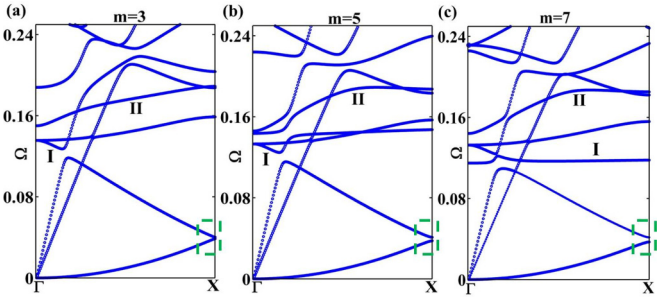

FIG. 11. (Color online) Dispersion relation for different taper exponent values: (a) $m = 3$, (b) 5, and (c) 7.

near points where their dispersion curves cross. The coupling causes a characteristic splitting of the dispersion curves at the crossing point while, elsewhere, the modes are essentially unaffected.

The other key design parameter is the exponential taper coefficient m. We consider a progression of the ABH profile from smooth (low m) to sharp (high m). For all cases, the residual thickness is maintained constant at $h_r = 0.0011$m by properly adjusting the coefficient ε. The dispersion relations are shown in Figs. 11(a)–11(c) for $m = 3$, 5, and 7. Of particular interest is the appearance of a band gap between the fundamental flexural mode A_0 and the negative branch of the fundamental nonmonotonous mode A_{0f} (see green dashed box) following the splitting of the folded A_0 mode. This band gap is related to the increased back-scattering occurring at large m where the ABH smoothness criterion is no more satisfied [20,23]. Overall, the higher frequency modes (above the fundamental) are more evidently affected by the change in the taper exponent. As an example, mode I and II show substantial changes as m increases. These two modes are characterized by monopolelike and dipolelike modal displacement fields inside the ABH and therefore are very sensitive to changes of the ABH profiles. Note also the formation (around $\Omega = 0.1244$) of a nearly flat band (mode I). This flat mode suggests the existence of a deaf band which does not couple with any external wave [46].

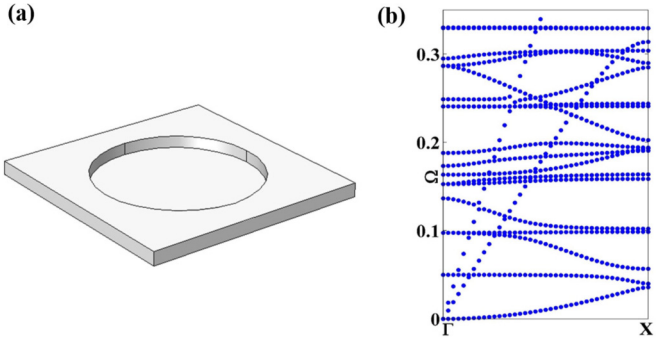

FIG. 12. (Color online) Dispersion relation for the limit case $\lim_{m\to\infty}$. (a) Schematic of the unit cell which tends to a cylindrical inclusion, and (b) dispersion relation showing that the coupling between the fundamental Lamb modes via the ZGVP disappears in the absence of the smooth ABH taper.

We observe that in the limit case of a large m coefficient ($\lim_{m\to\infty}$) that represents a very steep ABH unit, the configuration will tend to a cylindrical notch having the same radius and the same residual thickness [see Fig. 12(a)]. In this limit case, the ZGVP disappears leading to the typical decoupled fundamental Lamb modes S_0 and A_0. This result suggests that the cause of the ZGVP and of the correlated mechanisms, such as the negative bi-refraction, is in fact due to the specific geometry of the tapered inclusions. Nevertheless, we cannot exclude the existence of other tapered geometries exhibiting similar properties.

VII. CONCLUSIONS

In conclusion, we have introduced a class of two-dimensional nonresonant single-phase phononic crystals made of a periodic lattice of acoustic black holes. The remarkable dispersion characteristics of this material are of particular interest because obtained by exploiting an extremely simple design that does not require either the classical multi-phase material or the resonant structure approach. In addition, this design allows extending wave propagation mechanisms so far observed in periodic materials to thin-walled structural components therefore blurring the distinction between engineered materials and structures. Despite their outstanding simplicity, ABH-PCs provide the same plethora of wave propagation effects typically observed in locally resonant materials, including negative refraction, bi-refraction, Dirac cones, and mode hybridization. The intrinsic nature of the ABH-PC also allows extensive control of the propagation properties during the design phase by simply acting on the geometric parameters of the taper. It is expected that this type of structural materials could have critical applications for the development of high-performance thin-walled structures providing, as an example, unprecedented vibration and noise control capabilities.

[1] Z. Liu, X. Zhang, Y. Mao, Y. Zhu, Z. Yang, C. Chan, and P. Sheng, Science **289**, 1734 (2000).
[2] S. Yang, J. H. Page, Z. Liu, M. L. Cowan, C. T. Chan, and P. Sheng, Phys. Rev. Lett. **88**, 104301 (2002).
[3] H. Sanchis-Alepuz, Y. A. Kosevich, and J. Sanchez-Dehesa, Phys. Rev. Lett. **98**, 134301 (2007).
[4] D. Garcia-Pablos, M. Sigalas, F. M. de Espinosa, M. Torres, M. Kafesaki, and N. Garcia, Phys. Rev. Lett. **84**, 4349 (2000).
[5] J. Vasseur, P. Deymier, B. Chenni, B. Djafari-Rouhani, L. Dobrzynski, and D. Prevost, Phys. Rev. Lett. **86**, 3012 (2001).
[6] M. Torres, F. Montero de Espinosa, D. Garcia-Pablos, and N. Garcia, Phys. Rev. Lett. **82**, 3054 (1999).
[7] M. Kafesaki, M. Sigalas, and N. Garcia, Phys. Rev. Lett. **85**, 4044 (2000).
[8] A. Khelif, B. Djafari-Rouhani, J. Vasseur, and P. Deymier, Phys. Rev. B **68**, 024302 (2003).
[9] Y. Pennec, B. Djafari-Rouhani, J. Vasseur, A. Khelif, and P. Deymier, Phys. Rev. E **69**, 046608 (2004).
[10] Y. Pennec, B. Djafari-Rouhani, J. Vasseur, H. Larabi, A. Khelif, A. Choujaa, S. Benchabane, and V. Laude, Appl. Phys. Lett. **87**, 1 (2005).
[11] H. Zhu and F. Semperlotti, AIP Adv. **3**, 092121 (2013).
[12] H. Zhu and F. Semperlotti, J. Appl. Phys. **116**, 094901 (2014).
[13] F. Semperlotti and H. Zhu, J. Appl. Phys. **116**, 054906 (2014).
[14] M. Dubois, M. Farhat, E. Bossy, S. Enoch, S. Guenneau, and P. Sebbah, Appl. Phys. Lett. **103**, 071915 (2013).
[15] B. Morvan, A. Tinel, A. Hladky-Hennion, J. Vasseur, and B. Dubus, Appl. Phys. Lett. **96**, 101905 (2010).
[16] J. Pierre, O. Boyko, L. Belliard, J. Vasseur, and B. Bonello, Appl. Phys. Lett. **97**, 121919 (2010).
[17] T. Cui, D. Smith, and R. Liu, *Metamaterials: Theory, Design, and Applications* (Springer, New York, USA, 2009).
[18] S. H. Lee, C. K. Kim, C. M. Park, Y. M. Seo, and Z. G. Wang, *17th International Congress on Sound and Vibration 2010*, ICSV Vol. 1 (Curran Associates, Inc., Red Hook, NY, 2010), p. 170.
[19] C. Pekeris, J. Am. Acous. Soc. **18**, 295 (1946).
[20] M. Mironov, Sov. Phys. Acoust. **34**, 318 (1988).
[21] D. O'Boy, V. Krylov, and V. Kralovic, J. Sound Vib. **329**, 4672 (2010).
[22] V. Krylov and F. Tilman, J. Sound Vib. **274**, 605 (2004).
[23] P. A. Feurtado, S. C. Conlon, and F. Semperlotti, J. Acoust. Soc. Am. **136**, EL148 (2014).
[24] L. Zhao, S. C. Conlon, and F. Semperlotti, Smart Mat. Struct. **23**, 065021 (2014).
[25] Z. Hou and B. Assouar, Phys. Lett. A **372**, 2091 (2008).
[26] I. Tolstoy and E. Usdin, J. Acoust. Soc. Am. **29**, 37 (1957).
[27] X. Huang, T. T. Wu, and J. C. Hsu, Phys. Rev. B **79**, 104306 (2009).
[28] Y. Pennec, B. Djafari-Rouhani, H. Larabi, J. Vasseur, and A. Hladky-Hennion, Phys. Rev. B **78**, 104105 (2008).
[29] H. Pichard, A. Duclos, J.-P. Groby, V. Tournat, and V. E. Gusev, Phys. Rev. B **86**, 134307 (2012).
[30] M. Rupin, F. Lemoult, G. Lerosey, and P. Roux, Phys. Rev. Lett. **112**, 234301 (2014).
[31] V. Krylov, *Proceedings of International Conference on Computational Methods in Structural Dynamics and Earthquake Engineering, 13-16 June 2007, Rethymno, Crete, Greece (COMPDYN 2007)* (Rethymno, Crete, Greece, 2007).
[32] M. H. Lu, C. Zhang, L. Feng, J. Zhao, Y. F. Chen, Y. W. Mao, J. Zi, Y. Y. Zhu, S. N. Zhu, and N. B. Ming, Nat. Mater. **6**, 744 (2007).
[33] F. Liu, Y. Lai, X. Huang, and C. T. Chan, Phys. Rev. B **84**, 224113 (2011).
[34] D. Torrent and J. Sánchez-Dehesa, Phys. Rev. Lett. **108**, 174301 (2012).
[35] Y. Li, Y. Wu, and J. Mei, Appl. Phys. Lett. **105**, 014107 (2014).
[36] T. C. Wu, Y. Lai, Z. H. Hang, H. Zheng, and C. T. Chan, Nat. Mater. **10**, 582 (2011).
[37] R. A. Sepkhanov, Ya. B. Bazaliy, and C. W. J. Beenakker, Phys. Rev. A **75**, 063813 (2007).
[38] M. Diem, T. Koschny, and C. M. Soukoulis, Physica B **405**, 2990 (2010).
[39] X. Zhang, Phys. Rev. Lett. **100**, 113903 (2008).

[40] X. Zhang and Z. Liu, Phys. Rev. Lett. **101**, 264303 (2008).
[41] C. T. Chan, Z. H. Hang, and X. Huang, Adv. OptoElectron **2012**, 313984 (2012).
[42] Y. Wu, J. Li, Z. Q. Zhang, and C. T. Chan, Phys. Rev. B **74**, 085111 (2006).
[43] H. F. Talbot, No. IV, Philos. Mag. **9**, 401 (1836).
[44] Z.-G. Chen, X. Ni, Y. Wu, C. He, X.-C. Sun, L.-Y. Zheng, M.-H. Lu, and Y.-F. Chen, Sci. Rep. **4**, 4613 (2014).
[45] L. Solie and B. Auld, J. Acoust. Soc. Am. **54**, 50 (1973).
[46] J. Li and C. T. Chan, Phys. Rev. E **70**, 055602 (2004).